This article has been accepted for publication in a future issue of this journal, but has not been fully edited. Content may change prior to final publication.
IEEE TRANSACTIONS ON BIOMEDICAL ENGINEERING. PREPRINT VERSION. ACCEPTED JUNE, 2020

Design and Comparison of Magnetically-Actuated Dexterous Forceps Instruments for Neuroendoscopy

Andrew Lim, Adam Schonewille, Cameron Forbrigger, Thomas Looi, James Drake, Eric Diller

***Abstract*— Robot-assisted minimally invasive surgical (MIS) techniques offer improved instrument precision and dexterity, reduced patient trauma and risk, and promise to lessen the skill gap among surgeons. These approaches are common in general surgery, urology, and gynecology. However, MIS techniques remain largely absent for surgical applications with narrow, confined workspaces, such as neuroendoscopy. The limitation stems from a lack of small yet dexterous robotic tools. In this work, we present the first instance of a surgical robot with a direct magnetically-driven end effector capable of being deployed through a standard neuroendoscopic working channel (3.2 mm outer diameter) and operate at the neuroventricular scale. We propose a physical model for the gripping performance of three unique end-effector magnetization profiles and mechanical designs. Blocking force rates per external magnetic flux density were 0.309 N/T, 0.880 N/T, and 0.351 N/T for the three designs which matched the physical model's prediction within 14.9% error. The rate of gripper closure per external magnetic flux density had a mean percent error of 11.2% compared to the model. The robot's performance was qualitatively evaluated during a pineal region tumor resection on a tumor analogue in a silicone brain phantom. These results suggest that wireless magnetic actuation may be feasible for dexterously manipulating tissue during minimally invasive neurosurgical procedures.**

***Index Terms*—Medical Robotics, End Effectors, Micromanipulators, Neuroendoscopy, Micro/Nano Robots, Surgical Instruments**

I. Introduction

ROBOT-ASSISTED surgical approaches to minimally invasive surgeries (MIS) are used in a variety of surgical disciplines, notably gynecology, urology, orthopedic surgery, gastroenterology, and general surgery [1], [2]. Robot tools with articulated wrists offer surgeons greater dexterity, precision, and ergonomics over manual approaches. However, robot-assisted MIS remains largely absent in neurosurgical procedures, such as intraventricular neurosurgery [3].

Presently, intraventricular neurosurgery is performed manually using rigid endoscopes and non-wristed rigid instruments [4], [5], [6]. With existing techniques, surgeons must pivot their instruments using the surface of the patient's brain as a fulcrum to access certain intraventricular areas while ensuring that the tool contact does not damage healthy tissue walls [7]. The primary reason for the lack of robot-assisted MIS approaches in neurosurgery is the size of the available tools.

The size of available tools is presently limited by their mechanical transmissions. Most existing robotic surgical instruments rely on cable-actuated, rigid-joint mechanisms consisting of small, distally located pulleys that transform linear cable actuation into rotational wrist motion [8]. The da Vinci® Surgical System (Intuitive Surgical), which employs this type of mechanism, advertises 5 mm and 8 mm shaft diameters, with the 8 mm tools being the most commonly used [9]. Further miniaturization of this type of mechanism must overcome or avoid frictional inconsistencies (backlash and cable slip), fatigue issues, and loss of mechanical advantage making its viability for use in narrow MIS settings limited [8].

Continuum robots on the other hand are typically narrower, very dexterous robots and can facilitate reaching remote areas of the human body during MIS procedures by changing its tortuous path profile to avoid obstacles [10]. Such systems have been demonstrated in ophthalmic surgery [11], otolaryngology procedures [12], urologic surgery [13], [14], steerable catheters for cardiac surgery [15], [16], abdominal surgery [17], [18] and neurosurgery [19]. They present a feasible alternative to traditional rigid tool shafts in harder-to-reach locations. However, their end effectors are still often either non-dexterous or too large for neurosurgery. These robots may benefit greatly from an added dexterous end effector to carry out complicated procedures at otherwise inaccessible areas.

Magnetic actuation could present a viable alternative to existing cable-actuated end effector mechanisms at small-size scales and may be integrated easily with existing continuum robot tool shafts since no mechanical linkages are required from the end effector through the lumen of the tool. Magnetic robots consist of magnetic field manipulation systems, such as stationary or moving electromagnets and permanent magnets, combined with a magnetic end effector [20]. The end effector

*Research supported by the Canadian Institutes of Health Research grant #72055222 and the Natural Sciences and Engineering Research Council grant #72055331.

A. Lim, A. Schonewille, C. Forbrigger, J. M. Drake, and E. Diller are with the Department of Mechanical and Industrial Engineering, University of Toronto, Ontario, Canada (email: ediller@mie.utoronto.ca)

T. Looi, and J. M. Drake are with the Centre for Image Guided Innovation and Therapeutic Intervention (CIGITI), The Hospital for Sick Children, Toronto, Ontario, Canada

experiences forces and torques resulting from the magnetic field produced by the manipulation system. These attributes make magnetic actuation attractive from a medical perspective as it allows for remote control and navigation of small or tether-less microrobots and devices using wireless mechanical power transmission.

Existing medical applications for magnetic actuation are most commonly found for interventional cardiac procedures involving catheter navigation. Commercially available systems such as the Niobe system (Sterotaxis, Inc.) [21] and the Catheter Guidance Control and Imaging (CGCI) system (The Magnetecs Corporation) [22] can be used to magnetically steer catheters during endovascular procedures. Other magnetically-steered catheter devices have been demonstrated using a single distally-located magnet [23], multiple distally-located magnets [24], polymers infused with magnetic particles [25], a magnet tethered to the tip of the catheter via a string [26], a magnet fixed to the tip of a variable stiffness catheter [27], and a distally-mounted coil where active steering can be toggled in an MRI-guided device [28]. In other surgical disciplines, researchers have demonstrated capsule endoscopes for targeted drug delivery [29], magnetic robots for wireless drilling [30], MRI-controlled magnetic particles [31] MRI-powered robotic mechanisms [32], a device for painless colonoscopy [33], magnetic tissue retractors for abdominal surgery [34], and a magnetic suture device for tissue ligation and penetration [35]. However, these devices are designed for large open workspaces, for example the thorax or abdomen, or for procedures with a natural pre-guided path, and are therefore not suitable for small and narrow workspaces such as those found in neurosurgery. Dexterous magnetic grasping tools for these smaller workspaces remain largely unexplored.

In our previous work, a preliminary 4 mm-wide wristed grasping robot with three degrees-of-freedom (DOFs) was presented as a magnetic end effector within a stationary electromagnetic coil system [36]. A quasi-static simplified model for the end effector's flexible wrist was proposed and characterized, allowing for the design of an open-loop controller that could independently address the end effector's three degrees of freedom. Although this robot served as an informative proof-of principle prototype, its functionality as a feasible robotic surgical instrument for confined workspaces was limited by its inability to grasp objects larger than 2 mm across, its tool diameter, its thin gripping surfaces, and the small workspace of its magnetic manipulation system (40 mm x 40 mm x 20 mm). The design was not optimized for gripping performance and lacked a physical model of its behavior that included inter-magnetic forces which are important for the operation and design of the device.

In this work, we present an improved design of this surgical robot end effector and magnetic actuation system which addresses these limitations by optimizing the placement of the magnets to minimize the negative effects of inter-magnetic forces, scaling down the cross-sectional package to fit within a 3.2 mm circular channel, and increasing the end effector's ability to grasp larger objects. The robot we present consists of a permanent magnet end effector with flexible joints, a mechanically-driven tool shaft, and a rotating permanent magnet manipulation system. We examine the operational advantages and disadvantages of three unique and optimized end-effector magnetization profiles with regards to grasping force, number of DOFs, and anticipated difficulty of control. A model of inter-magnetic forces within the end effector is introduced which allows us to improve performance. We also introduce a magnetic field generation system which has a much larger opening (190 mm x 190 mm) and usable workspace (60 mm x 60 mm x 60 mm). We study the effectiveness of the three end effector designs by performing pineal region tumor resection surgeries on a silicone brain phantom.

II. Grasper Design

The three presented designs each function using a mechanistically unique principle (Fig. 1). It is necessary to study multiple designs as it is not clear which magnetization profile will perform the best due to the inherent tradeoffs each design has. The need to explore the grasping performance of

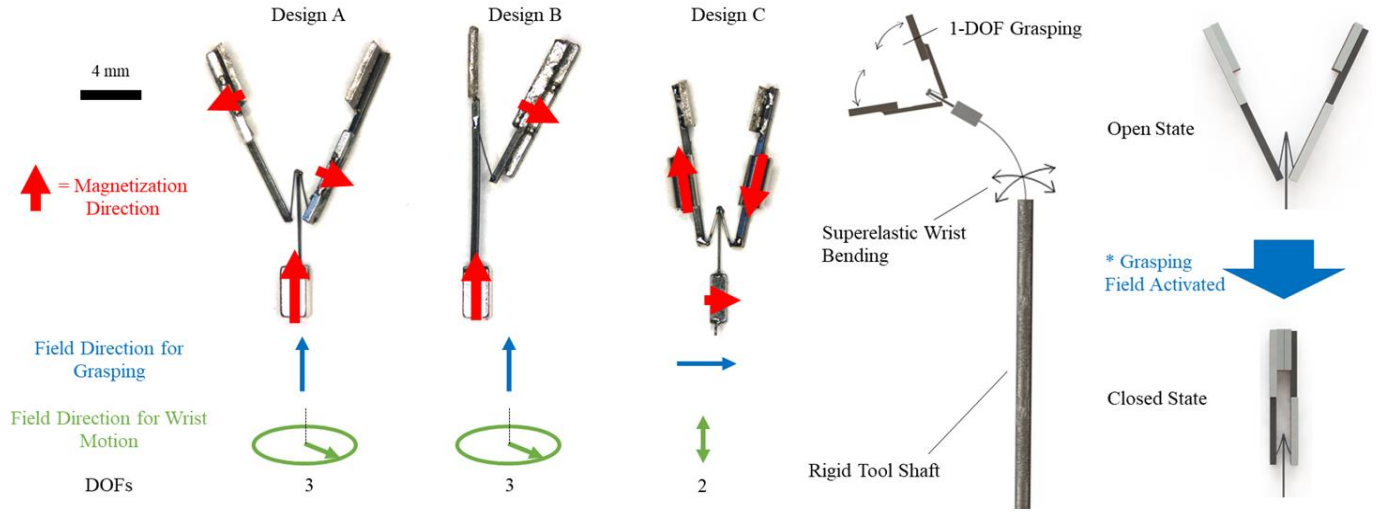

Fig. 1. Summary of magnetic forceps designs showcasing magnetization direction (red), the field direction required for grasping (blue), and the field direction required for deflecting the wrist (green). All designs house a different magnet configuration and rely exclusively on flexible joints.

each is therefore necessary. In our previous work [36], we characterized the wrist's response to different external magnetic fields. The wrist structure used in these three designs is identical to the wrist found in [36] as it proved to be capable of bending to nearly $\pm 90°$ using 10 mT of magnetic field strength. However, compared to our previous work [36], the grasping mechanisms have several significant improvements. First, the new designs fit within a 3.2 mm diametric constraint when the forceps are in a closed configuration: a 20% reduction in width from the previous design. Second, the new designs have a much larger grasping range, allowing for wider objects to be grasped. Last, the grasping digits have each been equipped with a large, rough grasping surface to increase the graspers' hold on soft objects. Fig. 1 shows a summary of the three new designs presented in this work.

A target grasping force of 1 N was chosen based on a study performed by Bekeny et al. on quantifying the forces applied at the skull base during transnasal endoscopic transsphenoidal tumor excision, a neuroendoscopic procedure [37]. Their study found that, among three patients, the average force at the base of the instrument was in the 0.10 N and 0.15 N range while the average maximum peak force experienced was 1.61 N. However, large forces were only experienced as collisions with bony tissue and the tool tip for a brief period of time. Most of the forces experienced were under 1 N.

With respect to each design's unique advantages and disadvantages, Design A is the most balanced from an overall magnetization perspective as its net magnetization always points distally and parallel to the wrist. It is a bipolar forceps mechanism where both grasping digits close symmetrically. However, the configuration of the grasping magnets is such that they repel each other naturally. As the device closes, this effect increases, leading to a lower effective grasping force. From this perspective, using large grasping magnets is a disadvantage. However, using large grasping magnets is also an advantage in that a larger torque can be generated by an external magnetic field due to the greater magnetic volume available for manipulation. Therefore, the amount of magnetic material used for this design must be carefully chosen to balance the grasper-closing torque generated by the external magnetic field and the grasper-opening torque generated by the inter-magnetic forces repelling the two grasping digits. Its wrist provides the tool with both pitch and yaw, adding much more surgical range than existing non-wristed instruments.

Design B works in a fundamentally similar manner to Design A. However, whereas as Design A features a bipolar forceps configuration, Design B uses a monopolar forceps mechanism. One of the grasping digits is rigid with respect to the wrist while the other is coupled to a flexible joint, allowing it to respond to external magnetic fields. With this design, there are no countering inter-magnetic forces as the forceps close, which allows for more magnetic material to be present on the device to maximize the total force transmission. Its wrist also features 2 DOFs. The drawback to this design is that grasper closure leads to a non-zero net torque generated on the distal tip causing issues with coupled grasper and wrist control.

Lastly, Design C attempts to leverage the inter-magnetic forces of the two grasping digits. Its magnets are configured such that the grasping digits attract rather than repel each other as the forceps close. However, due to the way these magnets must be configured, Design C's wrist can only have 1 DOF, hindering its range of motion. In Fig. 1, the field directions for grasping and wrist motion are outlined. Designs A & B have a distally oriented wrist magnet, allowing fields in the radial direction to manipulate the wrist's orientation. In Design C, the wrist magnet is oriented laterally, responding to fields in proximal-distal direction. This eliminates one of the wrist DOFs compared to Designs A & B. However, unlike Designs A & B's graspers which can only be actively closed using a uniform external magnetic field, Design C's grasper can be actively open and closed using a lateral field direction.

III. Modelling

In our previous work, a model for a magnetically-actuated flexible wrist was proposed and characterized to within 4% positional error [36]. This model was used as a foundation to model the flexible grasper joints. The previous model was able to capture the torque generated by the external magnetic field and the resistive torque generated by the wrist when it was deflected. However, the magnet used to actuate the wrist was sufficiently far from the magnets on the graspers and therefore the inter-magnetic torques and forces generated on the wrist magnet were negligible. For the proposed model of the new grasper designs, the magnets used for grasper actuation were non-negligibly close to each other which therefore required the consideration of the inter-magnetic dynamics.

Three torques are expected to play a role in grasper closure when actuating the device: the torque due to the external magnetic field on the permanent magnets, the elastic torque due to the flexible joint's deflection, and the inter-magnetic torque generated by the grasper magnets on each other. The theoretical contribution of each is summarized below.

A. External Magnetic Torque

In a uniform external magnetic field, each of the grasping magnets can be modelled using a single magnetic dipole moment. A torque, $\boldsymbol{T}_B$, is generated on this magnetic dipole moment according to,

$$\boldsymbol{T}_B = \boldsymbol{m} \times \boldsymbol{B}_{\text{ext}}, \tag{1}$$

where $\boldsymbol{m}$ represents the magnetic dipole moment of the magnet in the uniform magnetic field and $\boldsymbol{B}_{\text{ext}}$ represents the magnetic flux density of the external magnetic field. This is the torque that drives the method of actuation.

B. Elastic Torque due to Nitinol Joint Deflection

As the grasping digits deflect from its resting position, beam bending theory dictates that the restoring springs can be modelled as a cantilever in its linear-elastic region. Using this model, the resistive torque, $\boldsymbol{T}_k$, can be calculated as,

$$\boldsymbol{T}_k = k\theta\, \hat{\boldsymbol{k}}, \tag{2}$$

where k represents the angular bending stiffness of the restoring spring, θ represents angular deflection from the

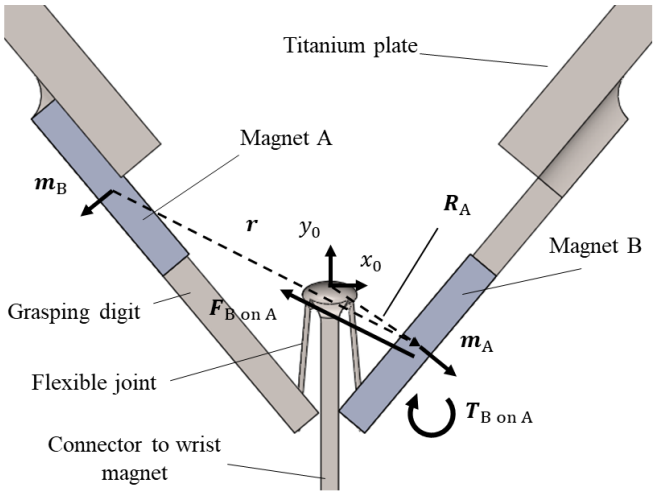

Fig. 2. Schematic of vector and frame definition for inter-magnetic dynamics of the grasper.

arm's resting orientation, and $\hat{\boldsymbol{k}}$ represents the unit vector pointed along the arm's rotational axis. Its direction is chosen to always try to restore the beam to its natural resting position. Furthermore, we can calculate the bending stiffness, k, as $\frac{EI}{L}$.

C. Inter-magnetic Torque

Lastly, since the grasping magnets may be non-negligibly close to each other in certain designs, a force and torque between the grasping magnets is generated. In general, a torque between two magnetic dipole moments is calculated as,

$$\boldsymbol{T}_{\mathrm{B\,on\,A}} = \frac{\mu_0}{4\pi r^5}[3\boldsymbol{m}_{\mathrm{A}} \times (\boldsymbol{m}_{\mathrm{B}} \cdot \boldsymbol{r})\boldsymbol{r} - r^2(\boldsymbol{m}_{\mathrm{A}} \times \boldsymbol{m}_{\mathrm{B}})], \quad (3)$$

where $\boldsymbol{m}_{\mathrm{A}}$ and $\boldsymbol{m}_B$ represent the two interacting magnetic dipole moments and $\boldsymbol{r}$ represents the vector from $\boldsymbol{m}_B$ to $\boldsymbol{m}_A$. These definitions are illustrated in Fig. 2. Furthermore, a force between two magnetic dipole moments is calculated as,

$$\boldsymbol{F}_{\mathrm{B\,on\,A}} = \frac{3\mu_0}{4\pi r^5}\left[(\boldsymbol{m}_{\mathrm{B}} \cdot \boldsymbol{r})\boldsymbol{m}_{\mathrm{A}} + (\boldsymbol{m}_{\mathrm{A}} \cdot \boldsymbol{r})\boldsymbol{m}_{\mathrm{B}} + (\boldsymbol{m}_{\mathrm{B}} \cdot \boldsymbol{m}_{\mathrm{A}}) - \frac{5(\boldsymbol{m}_{\mathrm{B}} \cdot \boldsymbol{r})(\boldsymbol{m}_{\mathrm{A}} \cdot \boldsymbol{r})}{r^2}\boldsymbol{r}\right]. \quad (4)$$

This force can be converted into a torque by taking the moment about the grasping mechanisms origin, represented by $\boldsymbol{T}_{f\,\mathrm{B\,on\,A}}$, and can be calculated according to,

$$\boldsymbol{T}_{f\,\mathrm{B\,on\,A}} = \boldsymbol{R}_{\mathrm{A}} \times \boldsymbol{F}_{\mathrm{B\,on\,A}}, \quad (5)$$

where $\boldsymbol{R}_{\mathrm{A}}$ represents the vector from the grasping mechanism's bending origin to the magnetic dipole moment $\boldsymbol{m}_{\mathrm{A}}$. Thus, the total inter-magnetic torque generated on $\boldsymbol{m}_{\mathrm{A}}$ by $\boldsymbol{m}_{\mathrm{B}}$ is the sum of $\boldsymbol{T}_{\mathrm{B\,on\,A}}$ and $\boldsymbol{T}_{f\,\mathrm{B\,on\,A}}$. These formulae can be used analogously for the interaction $\boldsymbol{m}_{\mathrm{A}}$ has on $\boldsymbol{m}_{\mathrm{B}}$ to generate equations for $\boldsymbol{T}_{\mathrm{A\,on\,B}}$ and $\boldsymbol{T}_{f\,\mathrm{A\,on\,B}}$.

However, since the magnetic volume is large in comparison to the distance between the interacting magnets, a simple single dipole model is insufficient. Rather, each permanent magnet volume must be split into N evenly spaced magnetic dipole moments where the i^{th} dipole moment, $\boldsymbol{m}_{\mathrm{A}_i} = \frac{\boldsymbol{m}_{\mathrm{A}}}{N}$. To determine the total torque experienced by $\boldsymbol{m}_{\mathrm{A}}$, the torque and force generated on each of the $\boldsymbol{m}_{\mathrm{A}_i}$ magnetic dipole moments by all of the N dipole moments $\boldsymbol{m}_{\mathrm{B}_i}$ on the second magnet must be considered and summed. For clarity, this is shown in Fig. 3 (a). Here, we must further show that with a sufficiently large N, the total inter-magnetic torque and force is stable. Fig. 3 (b) depicts this model using N ranging from 1 to 50. Notice that with low values of N, the net inter-magnetic torque magnitude tends to be unstable: small changes in N lead to large changes in the total inter-magnetic torque magnitude. However, as N becomes large, the total torque on $\boldsymbol{m}_{\mathrm{A}}$ converges asymptotically.

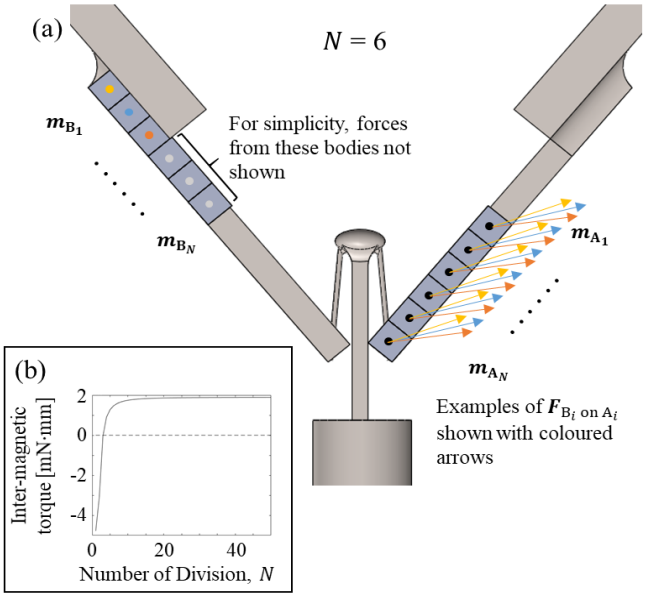

Fig. 3. (a) Schematic for an example of dividing the grasping magnets into N magnetic dipole moments. For simplicity, just a few interactions are shown. (b) Total inter-magnetic torque generated vs. the number of divisions, N.

D. Combining the Torques at Play

These torques may be summed to generate a net torque on each grasper according to equation (6).

$$\boldsymbol{T}_{\mathrm{net}} = \boldsymbol{T}_B + \boldsymbol{T}_k + \boldsymbol{T}_{\mathrm{B\,on\,A}} + \boldsymbol{T}_{f\,\mathrm{B\,on\,A}}. \quad (6)$$

By adding certain constraints to the device, experimentally testable relationships can be developed and characterized. First, consider the scenario where the devices are held fixed at a constant grasper closure angle, θ. Using these constraints, a relationship between θ and the external magnetic field magnitude, B_{ext} can be constructed as,

$$B_{ext}(\theta) = \frac{\left\|\boldsymbol{T}_k + \boldsymbol{T}_{\mathrm{B\,on\,A}} + \boldsymbol{T}_{f\,\mathrm{B\,on\,A}}\right\|}{m_{\mathrm{A}} \sin\theta}. \quad (7)$$

Notice that, at equilibrium, $\boldsymbol{T}_k$, $\boldsymbol{T}_{\mathrm{B\,on\,A}}$, and $\boldsymbol{T}_{f\,\mathrm{B\,on\,A}}$ are constants and therefore B_{ext} can be directly written with respect to θ.

Second, consider the scenario where θ is fixed at 0°. However, instead of considering the device at equilibrium, the net torque on the grasping digits may be taken as the cross-product between the moment arm from the origin of the

grasper to the force vector at the distal tip and the force exerted by the grasper at the distal tip as,

$$\boldsymbol{T}_{\text{net}} = \boldsymbol{R}_{\text{force}} \times \boldsymbol{F}_{\text{tip}}. \quad (8)$$

From equation (8), the force magnitude can be extracted as,

$$F_{\text{tip}} = \frac{T_{\text{net}}}{R_{\text{force}}}, \quad (9)$$

and the direction of the force can be taken as orthogonal to the grasping digit. Notice that with θ fixed, all the terms in equation (6) become constant with various external magnetic field strengths except for $\boldsymbol{T}_B$. Equations (7) and (9) offer relationships that were experimentally tested to validate this model.

IV. Experimental Setup

A. Fabrication

The specific placement and size of the magnets in each of the designs plays an important role in the overall net torque delivered by the graspers. For example, Design A's grasping magnets should be optimally sized and placed such that their repelling torques are minimized, but their volumes are large enough that a significant torque due to the external magnetic field can be applied. Therefore, the designs were optimized using the fitness function found in equation (6) using a brute force method that iterated over all possible combinations of magnet length(s) from 1 mm to 10 mm in increments of 0.5 mm and position(s) along their respective grasper arms in increments of 0.5 mm. The resultant structural parameters that resulted in the greatest net torque according to the fitness function were used as a target for each design. The geometric model proposed in section III was used to perform this optimization. The optimized parameters are summarized in Table I.

However, due to the irregular geometric shapes of the permanent magnets outlined by the model optimization, several smaller permanent magnets were laser welded together using the LaserStar iWeld 990 series laser welder to achieve the target geometry for Designs A and B. One drawback to this fabrication method is that because laser welding applies local heating well beyond the Curie temperature of the magnets, the magnets experience local demagnetization at the positions where the laser was fired. Therefore, to drastically mitigate this effect, the magnets were laser welded under an approximate 575 mT magnetic field in the direction of their magnetization using a 25.4 mm x 25.4 mm x 25.4 mm rare earth neodymium (NdFeB) permanent magnet to minimize this demagnetization effect. The use of this field during welding improved the magnetization retention from a mean 43.5% of the magnets' original strength to a mean 73.3% of the magnets' original strength among the magnets found in Designs A & B. Admittedly, this was not studied with rigor, but nonetheless, it suggests that using a magnetic substrate while welding reduces the negative effects of welding by approximately half.

TABLE I
Optimized and Actual Structural Parameters Used for Designs

Forceps Design		Magnet Volume [mm x mm x mm]	Grasper Length [mm]
A	Actual	6 x 1 x 0.0	12
	Optimized	5 x 1 x 0.5	10
B	Actual	9 x 1 x 0.5	10
	Optimized	10 x 1 x 1	10
C	Actual	1.59 diameter x 3.18 length	10
	Optimized	10 x 1 x 0.5	10

For Design A, the optimization process recommended placing a 5 mm x 1 mm x 0.5 mm magnet on each grasper digit. However, this magnet was particularly difficult to source or create. Instead, three 2 mm x 1 mm x 0.5 mm magnets were joined to create a 6 mm x 1 mm x 0.5 mm magnet. To compensate for this scaling up, the grasping digit length was also increased from 10 mm to 12 mm. The optimization process was repeated for this design with these new parameters to ensure the optimal configuration was selected.

For Design B, the optimization process recommended a 10 mm x 1 mm x 1 mm magnet. However, three 3 mm x 1 mm x 1 mm magnets were joined to generate a 9 mm x 1 mm x 1 mm magnet instead. Again, this choice was made out of convenience as a 10 mm x 1 mm x 1 mm magnet was difficult to source or create. Any combination of off-the-shelf magnets would have resulted in a minimum of four magnets being joined which would likely have amplified the demagnetization effect due to the additional number of laser weld spots required.

For Design C, sourcing magnets to the recommended size and magnetization direction was extremely challenging. Therefore, a slightly wider (diameter = 1.59 mm), cylindrical magnet was used. This cylindrical magnet was readily available off-the-shelf and is similar in volume to the target magnet predicted by model optimization ($6.30\,\text{mm}^2$ vs. $5.00\,\text{mm}^2$ for the cylindrical magnet and optimization magnet, respectively). The centers of the cylindrical magnets were placed in a location on the grasper arms that would cause a similar inter-magnetic torque to the torque predicted by the model to compensate for the extra magnetic volume. The models for all three designs were adjusted to account for these slight volume deviations. Table I shows a summary of the optimized and actual structural parameters used for the designs.

To begin the rest of the fabrication process, the grasping magnets were fixed to the Nitinol grasping digits using Gorilla Super Glue adhesive. This was left to cure at room temperature for two hours before further fabrication resumed. Once dry, a larger, 0.4 mm x 2 mm x 3 mm grade 5 titanium plate was laser welded to the grasping digits to provide a large, rough grasping surface. This was repeated to achieve the second grasping digit assembly.

Then, these digits were placed magnet-side down onto a steel fabrication substrate in the laser welder. The steel substrate allowed the grasping digit to remain temporarily fixed (via magnetic bonding) in the ideal orientation and position for distal tip assembly. The grasping digits, along with the wrist, were laser welded to complete the distal tip of

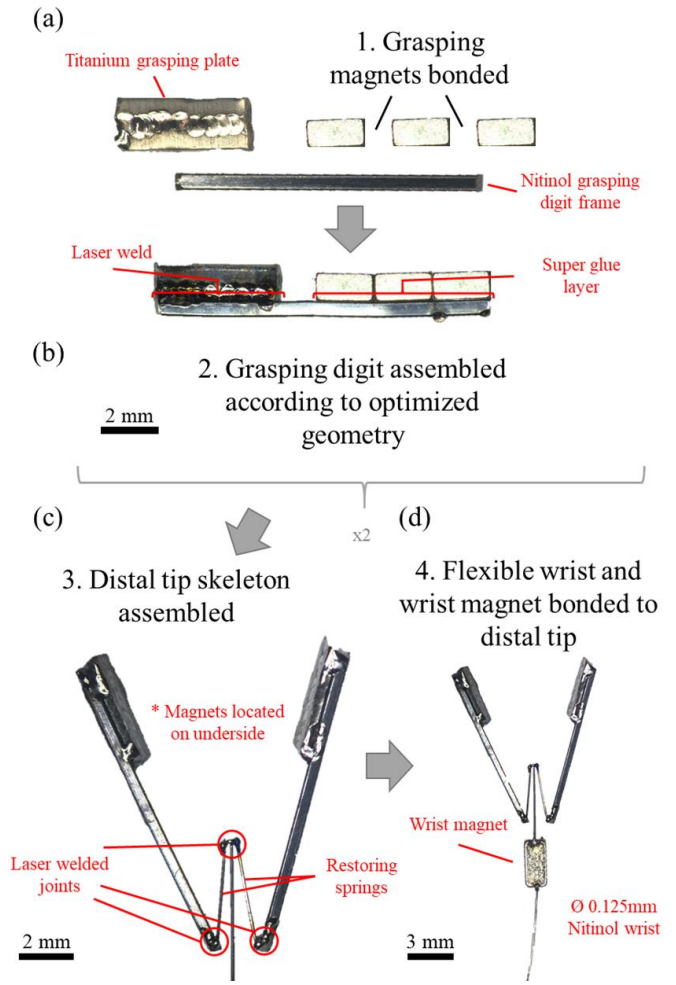

Fig. 4. Fabrication process overview. We begin by joining the necessary magnets to generate our target dimension (a). This is bonded to the grasping digit using an adhesive (b). All other joining in subsequent steps is performed by laser welding (c) & (d).

the device. It is important to note that with these designs, the inherent resting grasp range is much greater than our previous design found in [36], which consisted of two parallel grasping digits. All designs presented in this study have grasping digits in a structural configuration such that their distal ends are further apart than their proximal ends, allowing the device to grasp larger objects. In [36], the tip separation was approximately 2 mm whereas the mean tip separation of the presented devices is 6 mm.

The wrist magnet was then joined to the centre shaft on the distal tip and the wrist wire was joined to the proximal end of the wrist magnet. These steps were both completed using the laser welder. The final forceps assembly was carefully lifted from the steel plate, removing the temporary magnetic bond. Finally, the entire wrist was joined to a 30 cm rigid Nitinol tool shaft using a 24-hour Gorilla epoxy to create a full surgical forceps instrument. An overview of the fabrication process is outlined in Fig. 4.

B. Grasper Closure Angle vs. Magnetic Flux Density

To determine the accuracy of the proposed model for grasper closure, each of the three designs were placed into a system of 3 orthogonal pairs of Helmholtz coil pairs to deliver

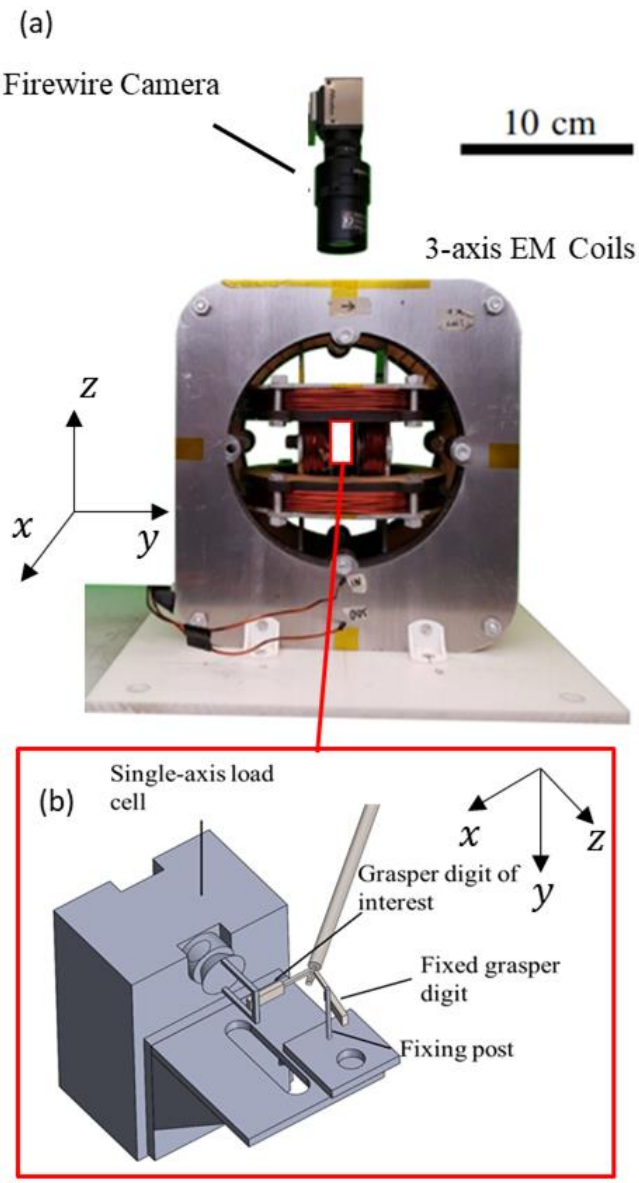

Fig. 5. (a) Three pairs of orthogonal Helmholtz coils capable of generating uniform magnetic flux density of 20 mT at its centre. (b) Experimental apparatus mock-up for block force testing. This apparatus was placed inside the centre of the Helmholtz coil pairs for precise magnetic flux density delivery.

a precise, uniform external magnetic field (Fig. 5 (a)). This is a 3-axis system of nested Helmholtz coil pairs, with one coil pair aligned with each of the x-, y-, and z-axes. The maximum continuous current in each coil is 15 A. The coil radii are 98 mm, 44 mm, and 69 mm for the x-, y-, and z-axes, respectively. The coils in each pair are spaced one radius apart. As a result, the inner uniform-field workspace is approximately a cubic volume with side length of 30 mm and a uniform external magnetic flux density of 20 mT may be delivered. An overhead FOculus FO124TC firewire camera at 60 frames per second was used to capture the grasper's closure angle over time as the system delivered up to 20 mT of external magnetic field in 1 mT increments of field strength. The relationship between grasper closure angle, θ, and the external magnetic flux density was compared to the predicted relationship from the proposed model in equation (7).

This article has been accepted for publication in a future issue of this journal, but has not been fully edited. Content may change prior to final publication.
IEEE TRANSACTIONS ON BIOMEDICAL ENGINEERING. PREPRINT VERSION. ACCEPTED JUNE, 2020

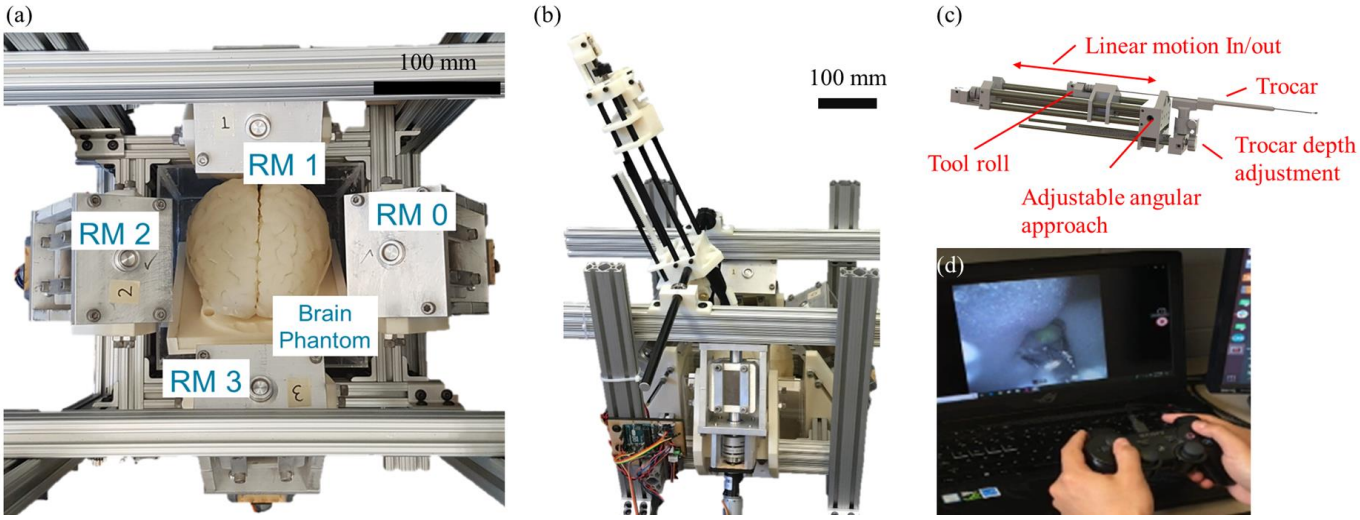

Fig. 6. (a)/(b) Permanent magnet system with four rotating magnets (RM) used to deliver controlled magnetic flux densities to the silicone brain phantom. (c) Tool base showcasing the additional DOFs it provides to the magnetic forceps. Also pictured are the 3D printed trocar and trocar holder for this setup so no manual intervention is required during the simulations. (d) A game controller and endoscopic visual feedback is used to control the magnetic field and mechanical DOFs of the forceps instrument.

C. Tip Force in a Uniform External Magnetic Field

Using the same method of external magnetic field delivery, the blocking force at the tip of each grasper was measured while the grasper was as close to its undeflected state as possible. This experimental setup for force data collection is shown in Fig. 5 (b). A Transducer Techniques GSO100 single-axis load cell (manufacturer stated accuracy = $\pm$ 0.1 mN) was used to measure the tip force of the grasper for each design. A magnetic flux density from 0 mT to 20 mT was applied to the grasper sample in increments of 1 mT. Once at 20 mT, the magnetic flux density was decreased to 0 mT in decrements of 1 mT. This cycle was repeated three times per cycle for each of the three proposed designs.

D. Pineal Region Tumor Resection Simulation on a Silicone Brain Phantom

To demonstrate the functional feasibility of the proposed devices in a clinically relevant environment, all three designs underwent pineal region tumor resection simulations performed on a silicone brain phantom that was cast in a mold using EcoFlex20. A cooked pea was used as a representation for the tumor due to its resemblance in shape and feel to human tumors of the same region according to author consultations with expert neurosurgeons. This model has been previously used as a training platform for neurosurgical fellows performing similar operations using existing techniques with manual tools. The coil system used for the grasper characterization experiments could not be used for the surgical simulations due to workspace volume limitations.

Therefore, based on the design in [38], a custom system for delivering the magnetic field was developed which consisted of four 50.8 mm x 50.8 mm x 50.8 mm NdFeB N52 permanent magnets was used to deliver an external magnetic field to the surgical workspace. This setup is shown in Fig. 6. In spherical coordinates, each magnet origin is at a radial distance of 20 cm from the workspace origin, at a zenith angle of 60°, and equally spaced azimuthally about the z-axis. The axes of rotation are pointed 30° from the vertical axis toward the centre. The polarization direction of the magnets is always orthogonal to its respective axis of rotation. At rest, the magnets' polarization vectors point in the tangential direction with respect to the surface of the 20 cm sphere, generating no effective magnetic field at the center of the workspace. This positioning allows for high accessibility; with an opening 190 mm x 190 mm wide, a human head can be accommodated in the workspace. Each of the four large permanent magnets is actuated by a brushed DC motor (with 3000 encoder steps per output revolution controlled by a closed-loop PID controller via Arduino Uno). The dipole model can be used to estimate the field produced by each magnet [39] and by rotating the magnets about their fixed axes, an external magnetic field with a strength of 0-20 mT can be delivered in three dimensions to the workspace. Due to the nonlinear relationship between the rotation angle of each permanent magnet and its resulting magnetic field contribution in the workspace, an iterative optimization procedure was used to determine the required permanent magnet rotation angles in real time. Gradient descent was used to determine the set of magnet rotation angles required to obtain the desired magnetic field. This method is derived from the optimization procedure found in [38].

The non-ferrous magnet fixtures and housings, along with a custom tool holder, were fixed to a rigid aluminum frame. The tool holder adds an extra four degrees of freedom to the tool including base height adjustment, tool entry angle, tool roll, and tool translation in/out of the workspace. This setup enhances the instrument's positional flexibility and stability. Furthermore, a 3D printed trocar and trocar holder were incorporated into this setup such that no external manual handling of the instrument was required for the resection simulations. The trocar was modelled after the Aesculap MINOP InVent Intraventricular Neuroendoscopy trocar. An Enable, Inc. Imaging Innovations (CA, USA) minnieScope®-XS flexible camera was used for all visualization to capture a real-time endoscopic view of the procedure during the simulations.

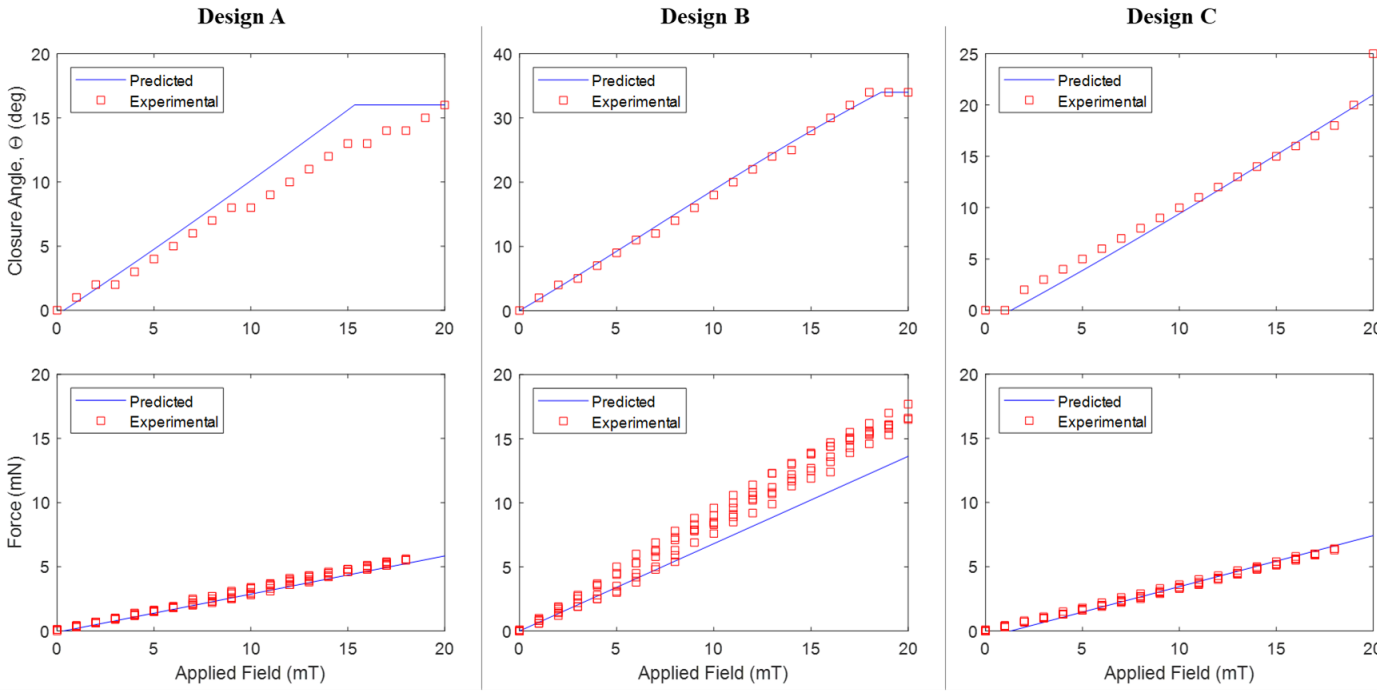

Fig. 7. (Top) Predicted and experimental data for closure angle, θ, vs. external magnetic flux density, B. (Bottom) Predicted and experimental data for tip force vs. external magnetic flux density, B.

Surgical simulations were performed by users who were not experienced in surgery but were familiar with the control of the tool. The silicone brain was placed in the system such that the third ventricle was centered in the workspace of the magnetic actuation system. Then, a cooked pea was placed in the pineal region of the silicone brain. The trocar was positioned into the brain at an angle similar to a manual surgical approach. Finally, the tool was deployed through the trocar into the third ventricle for tumor resection. All tool control was performed via human operation on a video game controller where the user may easily set the 3-dimensional magnetic flux density values of the system, the tool translation in and out of the workspace, the roll of the tool, and several other geometric parameters.

V. Results

A. Grasper Closure Angle vs. Magnetic Flux Density

A video was captured of each of the graspers' behavior in a uniform magnetic flux density from 0 mT to 20 mT in the direction of their respective grasper closure direction. The experimental and predicted degree of grasper closure, θ, vs. the applied external magnetic flux density magnitude, B, is shown in Fig. 7 (top).

For all three designs, the model predicts a linear trend for θ as the magnitude of magnetic flux density increases. The experimental data agrees with this trend reasonably well for Designs A and B. However, although Design C's experimental data is linear for most of its angular range, there is a sharp increase right at the very end of the grasper's closure which is a result of the attractive properties of Design C's configuration when the two magnets become very close. This attribute is not seen in the proposed closure model.

A summary of the slope line values for the model predictions and the experimental data is shown in Table II. This data shows that the mean percent difference in closure rate between the model and measured experimental values is 11.2% for all the designs.

B. Tip Force vs. Magnetic Flux Density

The proposed force prediction model from equation (9) was used to characterize the experimental force output of the grasper in an open configuration. The tip force for each of the three designs are shown against the external magnetic flux density magnitude, B, in Fig. 7 (bottom). The experimental loading and unloading points are shown with red markers and a solid blue line is shown to represent the predicted relationship determined using the model.

The loading and unloading of the grasper with magnetic flux density appears repeatable across the three loading/unloading cycles. Since the experimental data was collected using a blocking force, no hysteresis is expected. Similar to the grasper closure, the predicted and experimental slopes both appear linear. The mean percent difference between the predicted and experimental rates is 14.9%. Discrepancies may be attributable to the error in fabrication and/or error in skeleton dimension measurement. It is likely that as manufacturing becomes more consistent, the models and experimental data will reflect each other with greater

TABLE II
PREDICTED SLOPE VS. EXPERIMENTAL SLOPE FOR GRASPER CLOSURE, Θ, VS. EXTERNAL MAGNETIC FLUX DENSITY, B.

Forceps Design	Predicted Rate [°/T]	Experimental Rate [°/T]
A	1067	843
B	1873	1884
C	1138	1000

TABLE III
PREDICTED SLOPE VS. EXPERIMENTAL SLOPE FOR GRASPER FORCE VS. EXTERNAL MAGNETIC FLUX DENSITY, B.

Forceps Design	Predicted Rate [N/T]	Experimental Rate [N/T]
A	0.297	0.309
B	0.681	0.880
C	0.397	0.351
Previous 4 mm version [36]	N/A	0.290

accuracy. A summary comparing the predicted and experimental results along with an experimental comparison to our previous prototype are shown in Table III.

Furthermore, while the electromagnetic coil system used for these experiments was only capable of achieving magnetic fields up to 20 mT, a fixed 60 mT field was generated with large permanent magnets to measure the grip strength of Design B at full closure. The resulting measured force of 36.2 mN is very similar to our model's prediction of 37.0 mN which suggests that the lower field magnitude results can be extrapolated to higher field magnitudes.

C. Pineal Region Tumor Resection Simulation on a Silicone Brain Phantom

Human pineal region tumor resection simulations were performed with all designs. As predicted, each design had its own advantages and disadvantages in practice. Overall, all three designs were successfully able to remove the tumor analogue. Select frames from videos of the resections are shown in Fig. 8. These are shown from an endoscopic view, which is similar to a surgeon's view in the third ventricle during a neuroendoscopic procedure. Qualitative observations for each design are outlined below.

1) Design A

The magnet configuration of Design A allowed the user to quickly adapt to the control of the device. This is because the wrist control and grasping control are decoupled from one another; applying a magnetic flux density in the local orthogonal plane had strong effects on wrist bending but negligible effects on the closure of the grasper and the magnetic flux density in the local parallel direction had strong effects on grasper closure but negligible effects on wrist movement. For this reason, maneuvering the distal tip to the tumor analogue was simple.

However, due to the low magnetization strength of the grasping magnets, the maximum available local parallel magnetic flux density of the system was required to make contact around the tumor analogue. Many attempts were required before successful grasping of the tumor analogue was achieved.

2) Design B

Compared to Design A's simplistic control, Design B was noticeably much more difficult to control. Specifically, it was very apparent that magnetic flux densities in the local orthogonal plane or in the local parallel plane had significant effects on both grasper closure and wrist movement. This control coupling made navigation to the tumor analogue very difficult. However, once the resection site was reached, the grasping force was very strong, and fewer attempts at grasping were necessary for successful resection compared to Design A.

The reason for significant coupling between the wrist and grasping can be attributed to the unbalanced nature of the magnet configuration. The torques generated on Design A's grasping magnets are always balanced by each other leading to zero net torque on the distal tip. However, since there is only one grasping magnet in Design B, its grasping torque is not countered leading to coupled effects. Still, with more sophisticated control modelling, this challenge can likely be overcome.

3) Design C

Design C's configuration provided an intermediate performance between Design A and Design B. The wrist and grasping controls were very simple for the human operator to adjust to, requiring minimal user-training time. Grasping was strong and had the added flexibility of being able to open using a grasper magnetic flux density in the opposite direction without causing instability in the wrist orientation. This feature is not available for Designs A and B because the grasper magnetic flux density direction for opening the grasper produces an unstable equilibrium for the wrist.

However, the wrist's limitation of just 1 DOF in tool pitch made navigation to the resection site very challenging from a single angle of tool entry. Therefore, navigation required much more use of the mechanical roll feature from the tool base. This limitation may disqualify Design C from several applications where a particular wrist pitch or yaw angle approach would be required given the patient's anatomy. However, dissimilar to current neuroendoscopic techniques, it should be noted that these simulations were performed using a

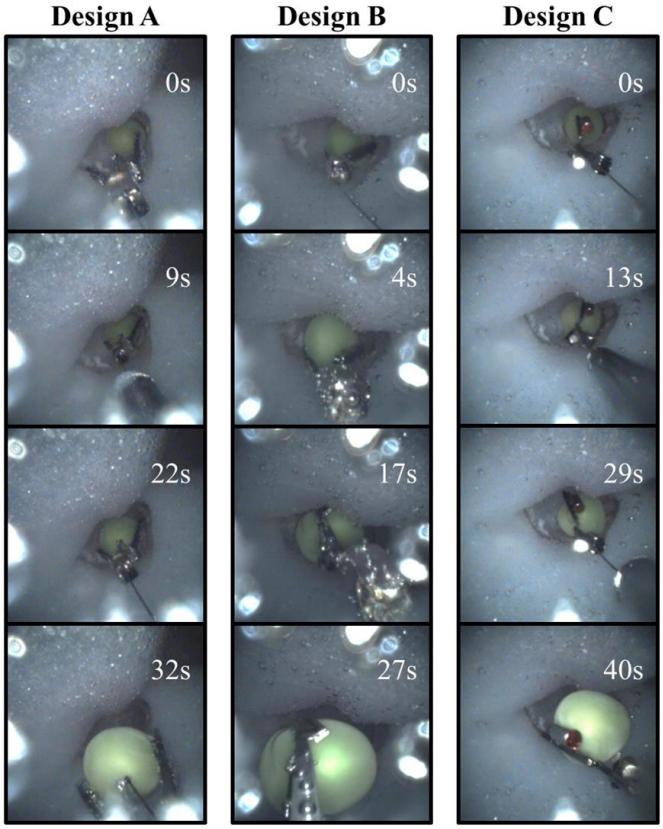

Fig. 8. Select frames from the tumor resection simulation in a silicone brain phantom for Designs A, B, and C. All forceps designs were successfully able to retract the tumor analogue using just endoscopic feedback.

single angle of tool entry. The ability to pivot the trocar and tool about the brain's surface may greatly improve the performance of Design C. Furthermore, one potential solution for adding another wrist DOF would be to employ magnetic-gradient-controlled DOFs, as opposed to relying exclusively on uniform magnetic flux density DOFs. At present, this is beyond the scope of these designs.

VI. Discussion

The proposed model framework agrees well with experimental data, yielding a mean error of 13.1% with respect to both grasping behaviors. Furthermore, the linear nature of both grasping behaviors is captured. This suggests that the framework may be used for future implementation into closed-loop control systems for better and more accurate grasper control. Furthermore, as the fabrication consistency and part standardization improve, it is likely that this model's performance will also improve.

The accuracy of these models also suggests that the dynamics at play are captured within the model and can therefore be extended to other magnet configurations since it has provided accurate comparisons for three different designs. This would allow for an accurate prediction of a configuration's performance before going through full prototype fabrication. Furthermore, this model will play a significant role in future closed-loop control for future systems.

From a grasper performance perspective, the 4 mm forceps had a force per magnetic flux density rate of 0.29 N/T [36]. These forceps were larger in width and had a smaller grasping range. All three of the optimized mechanisms had greater experimental force per magnetic flux density rates with a much wider grasping range and a smaller cross-sectional package. Therefore, the optimization process provided a means of organizing the configuration of the magnets such that the graspers had greater force output in a more compact design. Furthermore, the force rate of Design B's experimental and predicted data is nearly three times greater than Design A or Design C's force rates. Since force output is a known limitation for magnetically-actuated forceps mechanisms, Design B's potential as a feasible surgical robotic instrument is high. Through means of further geometric design optimization and fully preserving the magnetization of the magnets, it is expected that the force output for this design can be improved eight-fold in future designs while maintaining its compact physical size.

The resection simulations shown in this work demonstrate the feasibility of using magnetically-actuated devices for neuroendoscopic applications. The presented robotic instruments are small enough to safely be deployed through an existing neuroendoscopic trocar replica and perform simple resection tasks in a clinically representative environment. Although simple resection of a cooked pea tumor analogue could be achieved, the current capabilities of the proposed devices with the current system are likely inadequate from a force output perspective for performing all the surgical tasks necessary during a human neuroendoscopic procedure as the greatest force output was 17.6 mN using 20 mT of field strength. However, a stronger magnetic system, such as the 400 mT system showcased by Rahmer et al. [30], could significantly enhance our instruments by offering an estimated twenty-fold increase in grasping strength. Furthermore, a significant portion of the grasper skeleton is fabricated using nonmagnetic materials to simplify the fabrication process. If the fabrication process improves such that any magnetic geometry could be achieved, an estimated two- to four-fold increase in force output may be feasible. Still, the demonstration here was important for showcasing the added dexterity of the wrists for these instruments. The additional dexterity allowed for increased surgical reach, precision, and ultimately tumor analogue resection from just a single angle of tool entry. Unlike manual instruments, this eliminated the need to apply torque onto the brain's surface. Future efforts toward improving the magnetic manipulation system by increasing the magnetic field strength delivered over a workspace of similar or larger size for this robot will likely enable the utilization of magnetic instruments for more complex, more difficult surgical procedures.

From a magnetic field creation perspective, the field generation system shown here relies on the user's knowledge of the magnetization profiles of the tools to vary the field created and control the motion of the end effector. In particular, the user must have prior knowledge of which component of the magnetic field affects which DOF on the wrist. Therefore, from a usability standpoint, a surgeon, with no experience using the system, must mentally map the field directions to the kinematics of the tool. To improve this, the system's user interface will be designed in the future to include an inverse kinematics profile for each tool such that the user's controller will map directly to the pitch angle, yaw angle, and grasper closing strength of the tool. For the work presented here, an integrated inverse kinematics controller was not required as the operators of the device in this study had significant prior knowledge of how the external magnetic field specifically affected the operation of the devices. However, with minor modifications to account for tool entry angle and anatomical variability, the existing wrist and grasper models are capable of feasible implementation of a simple mapping method for Designs A & C in future implementations. On the other hand, because Design B experiences coupled effects between the wrist and grasper control, further investigation into its mechanics is required.

Lastly, to improve the user's intuition for the control, a future system may benefit from the use of a user interface that more closely mimics a wrist mechanism. An example of a user interface that could improve usability is an omni-directional pen controller that senses the orientation of the user's wrist (e.g. Geomagic Touch™ from Quanser). This wrist information could be used to control the tool's wrist orientation.

VII. Conclusion

This study presents the design, characterization, and mock-surgical performance of several of the first instances of a magnetically actuated forceps instrument for neurosurgery. The developed geometric models accurately predict the performance of each proposed forceps grasper mechanism. While the force output of the graspers using the magnetic

delivery systems in this study are not feasible for neuroendoscopy in its current form, we anticipate that this challenge could be overcome using a stronger existing magnetic delivery system. This study also showcases a successful tumor resection surgical simulation in a silicone adult-sized brain phantom with each forceps design. Further development of these instruments may improve neuroendoscopic outcomes by allowing for greater surgical precision, dexterity, and efficiency.

REFERENCES

[1] J. Doulgeris, et al., "Robotics in Neurosurgery: Evolution, Current Challenges, and Compromises," *Cancer Control*, vol. 22, no. 3, pp. 352-9, 2015.

[2] P. McBeth, et al., "Robotics in neurosurgery," *Amer. J. Surgery*, vol. 188, no. 4A Suppl, pp. 68S-75S, 2004.

[3] H. J. Marcus, et al., "da Vinci robot-assisted keyhole neurosurgery: a cadaver study on feasibility and safety," *Neurosurgery Rev.*, vol. 38, no. 2, pp. 367-71, 2015.

[4] F. Ahmad and D. Sandberg, "Endoscopic Management of Intraventricular Brain Tumors in Pediatric Patients: A Review of Indications, Techniques, and Outcomes," *J. Child Neurology*, vol. 25, no. 3, pp. 359-67, 2010.

[5] K. Shim, et al., "Neuroendoscopy: Current and Future Perspectives," *J. Korean Neurosurgery Soc.*, vol. 60, no. 3, pp. 322-326, 2017.

[6] M. Gaab, "Instrumentation: Endoscopes and equipment," *World Neurosurgery*, vol. 79, no. 2 Suppl, pp. S14.e11-21, 2013.

[7] B. G. Rocque, "Neuroendoscopy for Intraventricular Tumor Resection," *World Neurosurgery*, vol. 90, pp. 619-620, 2016.

[8] H. Le, T. Do and S. Phee, "A survey on actuators-driven surgical robots," *Sensors and Actuators A: Physical*, vol. 247, pp. 323-54, 2016.

[9] Intuitive Surgical, Inc., "Intuitive Surgical Annual Report," 2018.

[10] J. Burgner-Kahrs, D. C. Rucker, and H. Choset, "Continuum Robots for Medical Applications: A Survey," *IEEE Transactions on Robotics*, vol. 31, No.6, pp. 1261-1280, 2015.

[11] H. Yu, et al., "Design, calibration and preliminary testing of a robotic telemanipulator for OCT guided retinal surgery," in *Proc. IEEE Int. Conf. Robot. Autom.*, 2013, pp. 225–231.

[12] J. Burgner, et al., "A telerobotic system for transnasal surgery," *IEEE/ASME Trans. Mechatronics*, vol. 19, no. 3, pp. 996–1006, 2014.

[13] R. E. Goldman, A. Bajo, L. S. MacLachlan, R. Pickens, S. D. Herrell, and N. Simaan, "Design and performance evaluation of a minimally invasive telerobotic platform for transurethral surveillance and intervention," *IEEE Trans. Biomed. Eng.*, vol. 60, no. 4, pp. 918–25, 2013.

[14] R. J. Hendrick, S. D. Herrell and R. J. Webster III, "A multi-arm handheld robotic system for transurethral laser prostate surgery," in *Proc. IEEE Int. Conf. Robot. Autom.*, 2014, pp. 2850–2855.

[15] S. B. Kesner and R. D. Howe, "Position control of motion compensation cardiac catheters," *IEEE Trans. Robot.*, vol. 27, no. 6, pp. 1045–1055, 2011.

[16] A. H. Gosline, et al., "Percutaneous intracardiac beating-heart surgery using metal MEMS tissue approximation tools," *Int. J. Robot. Res.*, vol. 31, no. 9, pp. 1081–1093, 2012.

[17] J. Ding, et al., "Design and Coordination Kinematics of an Insertable Robotic Effectors Platform for Single-Port Access Surgery," *IEEE/ASME Transactions on Mechatronics*, Vol. 18, No.5, pp. 1612-1624, 2013.

[18] K. Xu, J. Zhao, and M. Fu, "Development of the SJTU Unfoldable Robotic System (SURS) for Single Port Laparoscopy," *IEEE/ASME Transactions on Mechatronics*, Vol. 20, No.5, pp. 2133-2145, 2015.

[19] J. A. Engh, et al., "Percutaneous intracerebral navigation by duty-cycled spinning of flexible bevel-tipped needles." *Neurosurgery*, vol. 67, no. 4, pp. 1117-1122, 2010.

[20] J. J. Abbott, E. Diller and A. J. Petruska, "Magnetic Methods in Robotics," *Annu. Rev. Robot. Cont. Autom.*, vol. 3, no. 1, 2020.

[21] F. Carpi and C. Pappone, ""Stereotaxis Niobe® Magnetic Navigation System for Endocardial Catheter Ablation and Gastrointestinal Capsule Endoscopy," *Expert Rev. Med. Devices*, vol. 6, no. 5, pp. 487-98, 2009.

[22] E. S. Gang, et al., "Initial Animal Validation of a New Remote Electrophysiology Catheter Guidance and Control System," *Circulation: Arrhythmia and Electrophysiology*, vol. 4, no. 5, pp. 770-7, 2011.

[23] S. Jeon, et al., "Improving guidewire-mediated steerability of a magnetically actuated flexible microrobot," *Micro and Nano Syst. Letters*, vol. 6, no. 15, 2018.

[24] S. Jeon, et al., "A Magnetically Controlled Soft Microrobot Steering a Guidewire in a Three-Dimensional Phantom Vascular Network," *Soft Robotics*, vol. 6, no. 1, pp. 54-68, 2019.

[25] Y. Kim, et al., "Ferromagnetic soft continuum robots," *Science Robotics*, vol. 4, no. 33, 2019.

[26] C. Chautems and B. J. Nelson, "The tethered magnet: Force and 5-DOF pose control for cardiac ablation," *2017 IEEE International Conference on Robotics and Automation (ICRA)*, Singapore, 2017, pp. 4837-4842, doi: 10.1109/ICRA.2017.7989562.

[27] C. Chautems, et al., "A variable stiffness catheter controlled with an external magnetic field," *2017 IEEE/RSJ International Conference on Intelligent Robots and Systems (IROS)*, Vancouver, BC, 2017, pp. 181-186, doi: 10.1109/IROS.2017.8202155.

[28] A. D. Losey, et al., "Magnetically Assisted Remote-controlled Endovascular Catheter for Interventional MR Imaging: In Vitro Navigation at 1.5 T versus X-ray Fluoroscopy," *Radiology*, vol. 271, no. 3, pp. 862-9, 2014.

[29] F. Carpi, et al., "Magnetically Controllable Gastrointestinal Steering of Video Capsules," *IEEE Trans. Biomed. Eng.*, vol. 58, no. 2, pp. 231-34, 2011.

[30] J. Rahmer, C. Stehning and B. Gleich, "Remote magnetic actuation using a clinical scale system," *PLoS ONE*, vol. 13, no. 3, 2018.

[31] S. M. Jeon, et al., "Precise manipulation of a microrobot in the pulsatilke flow of human blood vessels using magnetic navigation system," *J. Appl. Phys.*, vol. 109, no. 7, pp. 07B3A6, 2011.

[32] O. Felfoul, et al., "Achieving commutation control of an MRI-powered robot actuator," *IEEE Trans. Robot.*, vol. 31, no. 2, pp. 387-99, 2015

[33] P. Valdastri, et al., "Magnetic air capsule robotic system: proof of concept of a novel approach for painless colonoscopy," *Surg. Endosc.*, vol. 26, pp. 1238-46, 2012.

[34] N. Garbin, et al., "Laparoscopic tissue retractor based on local magnetic actuation," *J. Med. Devices*, vol. 9, no. 1, pp. 011005, 2018.

[35] L. O. Mair, et al., "MagnetoSuture: Tetherless Manipulation of Suture Needles," *IEEE Transactions on Medical Robotics and Bionics*, vol. 2, no. 2, pp. 206-215, May 2020, doi: 10.1109/TMRB.2020.2988462.

[36] C. Forbrigger, et al., "Cable-less, Magnetically-Driven Forceps For Minimally Invasive Surgery," *IEEE Robot. & Automat. Letters*, vol. 4, no. 2, pp. 1202-7, 2019.

[37] J. R. Bekeny, et al., "Forces Applied at the Skull Base during Transnasal Endoscopic Transsphenoidal Pituitary Tumor Excision," *J. Neurol. Surg. B. Skull Base*, vol. 74, no. 6, pp. 337-41, 2013.

[38] P. Ryan and E. Diller, "Magnetic Actuation for Full Dexterity Microrobotic Control Using Rotating Permanent Magnet," *IEEE Trans. Rob.*, vol. 33, no. 6, pp. 1398-409, 2017.

[39] A. J. Petruska and J. J. Abbott, "Optimal Permanent-Magnet Geometries for Dipole Field Approximation," *IEEE Trans. Magnetics*, vol. 49, no. 2, pp. 811-19, 213.